Lab on a Chip

Remotely tunable microfluidic platform driven by nanomaterial-mediated on-demand photothermal pumping

Journal:	*Lab on a Chip*
Manuscript ID	LC-ART-03-2020-000317.R2
Article Type:	Paper
Date Submitted by the Author:	09-May-2020
Complete List of Authors:	Fu, Guanglei; Ningbo University, aBiomedical Engineering Research Center, Medical school Zhou, Wan; University of Texas at El Paso, Department of Chemistry and Biochemistry Li, XiuJun; University of Texas at El Paso, Chemistry ;

Lab on a Chip

PAPER

Remotely tunable microfluidic platform driven by nanomaterial-mediated on-demand photothermal pumping

Received 00th January 20xx,
Accepted 00th January 20xx

DOI: 10.1039/x0xx00000x

Guanglei Fu, ‡ [a,b] Wan Zhou, ‡ [a] and XiuJun Li *[a,c,d,e]

The requirement of on-demand microfluidic pumps and instrument-free readout methods remains major challenges for the development of microfluidics. Herein, a new type of microfluidic platform, an on-demand photothermal microfluidic pumping platform, has been developed using the on-chip nanomaterial-mediated photothermal effect as the novel and remotely tunable microfluidic driving force. The photothermal microfluidic pumping performance can be adjusted remotely by tuning the irradiation parameters, without changing on-chip parameters or replacing enzyme or other reagents. In contrast to graphene oxide, Prussian blue nanoparticles with stronger photothermal conversion efficiency were used as the model photothermal agent to demonstrate the proof of concept. The on-chip pumping distance is linearly correlated with both the irradiation time and the nanomaterial concentration. The applications of the photothermal microfluidic pumping have been demonstrated in multiplexed on-chip transport of substances such as gold nanoparticles and visual quantitative bar-chart detection of cancer biomarkers without using specialized instruments. Upon the contact-free irradiation by a laser pointer, the strong on-chip nanomaterial-mediated photothermal effect can serve as a robust and remotely tunable microfluidic pump in a PMMA/PDMS hybrid bar-chart chip to drive ink bars in a visual quantitative readout fashion. This is the first report of the photothermal microfluidic pumping platform, which has great potential for various microfluidic applications.

Introduction

Microfluidics has emerged as an increasingly attractive technology for point-of-care testing (POCT), especially in the fields of medical diagnostics, food and drug safety inspection, and environmental surveillance,[1-6] because of their outstanding merits of affordability, simplicity, portability, and high-throughput measurement.[7-13] Despite great research progress in microfluidics after more than two decades of development,[14-16] microfluidic platforms are still confronted with several major challenges.[17] In particular, the requirement of external microfluidic pumping accessories, such as pneumatic syringe pumps, usually results in higher cost, additional space, and operational complexity.[7, 17] Additionally, the assay readouts of these microfluidic chips usually rely on bulky and costly instruments and detectors, such as fluorescence microscopes, electrochemical working stations, and microplate readers.[18, 19] All these pumping and detection accessories have significantly compromised the inherent advantages of high portability and integrability and low cost from microfluidic systems.

Among various microfluidic analytical devices, volumetric bar-chart chips (V-Chips) have attracted great research attention particularly for quantitative POCT.[17, 20-23] One of the most promising features of these V-Chips is that the assay results can be quantitatively displayed as visual bar charts without the aid of complex analytical instruments.[17, 22] Based on the volumetric measurement of enzyme- or nanoparticle-catalyzed gas (*e.g.*, O_2) production that acts as the microfluidic pump of the dye movement, different types of V-Chips have been developed for quantitative detection of various disease biomarkers and pathogens.[20, 24-26] However, several limitations are usually encountered in these V-Chips, such as relatively low operational stability because of inevitable denaturation of enzymes, dependence of the catalytic activity on surrounding environments, and imprecise spatiotemporal controllability due to intrinsic properties of the enzyme- or nanoparticle-catalyzed reactions.[23] Therefore, more robust, stable, on-demand, adjustable, and multiplexed microfluidic pumping systems are highly needed to be integrated into bar-chart chips.

The integration of classic physical principles in microfluidics has provided new possibilities to develop novel microfluidic platforms.[22] Nanomaterial-mediated photothermal effects have been the subject of intensive research due to the unique light-to-heat photo-physical conversion property.[27-29] Currently, the near-infrared (NIR) laser-driven photothermal effect has been widely applied for photothermal therapy of cancers.[27, 30-34] A number of nanomaterials that can convert NIR light into heat have been developed as photothermal agents, such as carbon-, gold- and Prussian blue (PB)-based nanomaterials.[27, 35-

[a] Department of Chemistry and Biochemistry, University of Texas at El Paso, 500 West University Ave, El Paso, Texas, 79968, USA. E-mail: xli4@utep.edu
[b] Biomedical Engineering Research Center, Medical School of Ningbo University, Ningbo, Zhejiang, 315211, P. R. China.
[c] Biomedical Engineering, University of Texas at El Paso, 500 West University Ave, El Paso, Texas, 79968, USA.
[d] Border Biomedical Research Center, University of Texas at El Paso, 500 West University Ave, El Paso, Texas, 79968, USA.
[e] Environmental Science and Engineering, University of Texas at El Paso, 500 West University Ave, El Paso, Texas, 79968, USA.
† Electronic Supplementary Information (ESI) available: Details of the chip designs and the platform setup. See DOI: 10.1039/x0xx00000x
‡ These authors contribute equally to this work.

[41] Significantly, by using a portable laser pointer as the light resource with remotely tunable irradiation parameters, rapid and substantial heat production can be simply achieved as a result of the nanomaterial-mediated photothermal effect,[40] making it particularly promising to develop new point-of-care bioassays using a thermometer as the signal reader,[40-42] or serve as the novel on-demand microfluidic driving force. Our group has originated multiple nanomaterial-mediated photothermal immunosensing systems for quantitative biochemical analysis.[40, 41, 43] However, to the best of our knowledge, the nanomaterial-mediated photothermal effect has not been exploited in microfluidic pumping, especially in bar-chart chips.

Herein, we developed a new type of microfluidic pumping platform, a tunable on-demand photothermal microfluidic pumping platform, using the on-chip nanomaterial-mediated photothermal effect as the new microfluidic driving force. The nanomaterial-mediated photothermal effect was explored as the microfluidic pump in a PMMA/PDMS (Poly(methyl methacrylate)/Polydimethyl-siloxane) hybrid photothermal bar-chart chip (PT-Chip) to propel on-chip ink-bar-chart movement in a visual quantitative readout fashion, as shown in Scheme 1A. Two types of photothermal agents, PB NPs and graphene oxide (GO), were used to study the feasibility of the photothermal microfluidic pump. Upon the contact-free irradiation of the nanomaterial suspensions on the PT-Chip by an 808 nm laser, the on-chip photothermal effect results in rapid and substantial heat production. The subsequent heating of solutions leads to the rapid accumulation of vapor pressure in limited volumes of the inlets, thereby pumping the on-chip visual bar-chart movement of the nanomaterial suspensions. On-chip photothermal effects of the nanomaterials were investigated in three PT-Chips (Fig. S1-2) to demonstrate the proof of concept of the photothermal microfluidic pumping platform. Furthermore, we have exemplified its application for multiplexed on-chip transport of substances, such as gold nanoparticles (AuNPs) as shown in Scheme 1B, and visual quantitative readout of immunoassay signals in the photothermal bar-chart chip. To the best of our knowledge, this is the first attempt to exploit the nanomaterial-mediated photothermal effect for microfluidic pumping and also serves as the first report of the photothermal bar-chart microfluidic pumping platform, with potential for various microfluidic applications, especially for visual quantitative POCT.

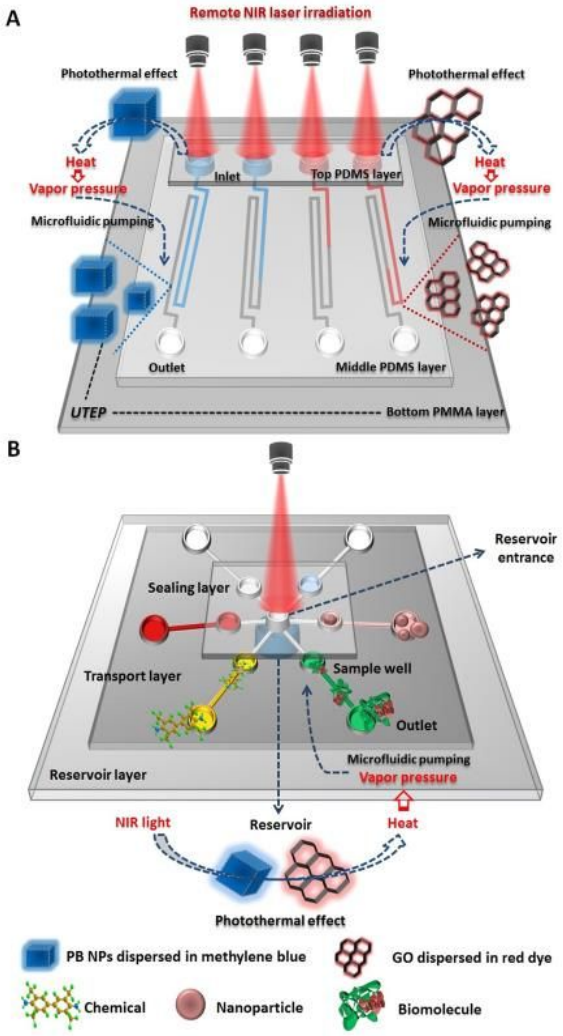

Scheme 1 Schematic illustration of (A) the photothermal microfluidic bar-chart chip using the on-chip nanomaterial-mediated photothermal effect as the microfluidic driving force and (B) multiplexed on-chip transport of substances using the photothermal microfluidic pumping.

Results and discussion

Off-chip investigation on photothermal effects of the nanomaterials

As a new generation of NIR laser-driven photothermal agents with strong photothermal conversion efficiency,[35] PB NPs were herein selected as the model photothermal agent in contrast to a typical kind of photothermal agent, GO.[44, 45] In comparison with methylene blue (MB) and red food dye (RD) as the blank dye indicators, the off-chip photothermal effects of the nanomaterials in the presence of the dye indicators were investigated before the on-chip photothermal study. UV-Vis absorption spectrometry was utilized to characterize the optical absorption properties of the nanomaterials in the NIR region as shown in Fig. 1. Typically, a broad absorption band from 450 nm to 900 nm was observed in the UV-Vis absorption spectra of PB NPs with a strong absorption peak at 715 nm, which can be attributed to the charge transfer transition between Fe(II) and

Fe(III) in PB NPs.[35, 46] Strong optical absorption of PB NPs in the NIR region after 800 nm was still observed, whereas both MB and RD showed no apparent absorption after 750 nm. As a classic kind of carbon-based photothermal agent, GO also exhibited distinct optical absorption in the NIR region but with significantly lower absorbance than PB NPs at the same concentration. The molar extinction coefficient of PB NPs at 808 nm (1.09×10^9 M^{-1} cm^{-1}) was reported to be several orders of magnitude higher than that of carbon-based nanomaterials (7.90×10^6 M^{-1} cm^{-1}).[35]

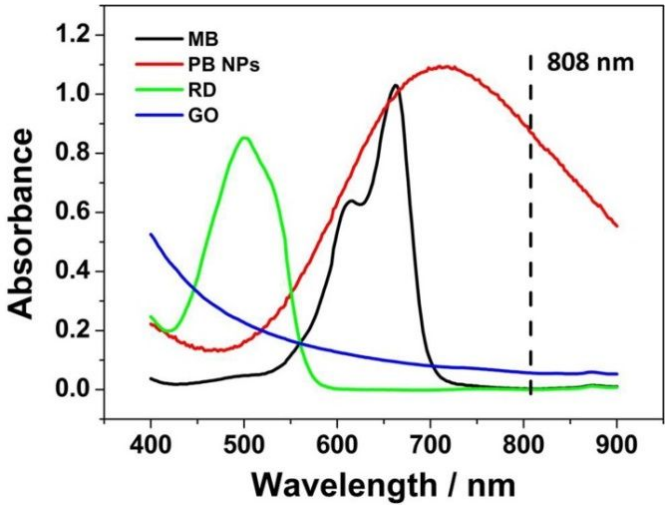

Fig. 1 Optical absorption properties of nanomaterials and dye indicators in the NIR region. UV-Vis absorption spectra of methylene blue (MB, 0.0125 mg·mL^{-1}), red food dye (RD), PB NPs (0.1 mg·mL^{-1}) and GO (0.1 mg·mL^{-1}) aqueous suspensions.

To further confirm the photothermal effect of the nanomaterials and study the effect of the dye indicators (i.e. MB and RD) on the photothermal responses, the off-chip photothermal effects of the nanomaterials in the presence of the dye indicators were investigated by employing an 808 nm diode laser as the NIR light source. Fig. 2A-B shows the temperature changes of the nanomaterial suspensions and the blank dye solutions during the horizontal laser irradiation process of 10 min. A digital thermometer was inserted into the suspensions to record the temperature. As expected, both PB NPs and GO suspensions exhibited dramatically temperature increases in a concentration-dependent manner during the irradiation process, whereas only minor temperature increases of less than 2.0 °C were observed from the blank dye solutions. The results indicated the intrinsically poor NIR laser-driven photothermal effect of MB and RD owing to their weak optical absorption in the NIR region as demonstrated in Fig. 1. PB NPs at a low concentration of 0.01 mg·mL^{-1} resulted in a drastic temperature elevation of 10.5 °C after the irradiation. Irradiation of the PB NPs suspension at a concentration of 0.03 mg·mL^{-1} for only 1.0 min led to a rapid temperature increase of 5.5 °C. In contrast to PB NPs, GO with a 10-fold higher concentration exhibited a much slower temperature elevation rate than PB NPs at each concentration, suggesting a stronger NIR laser-driven photothermal effect of PB NPs than GO because of the higher molar extinction coefficient of PB NPs at 808 nm.

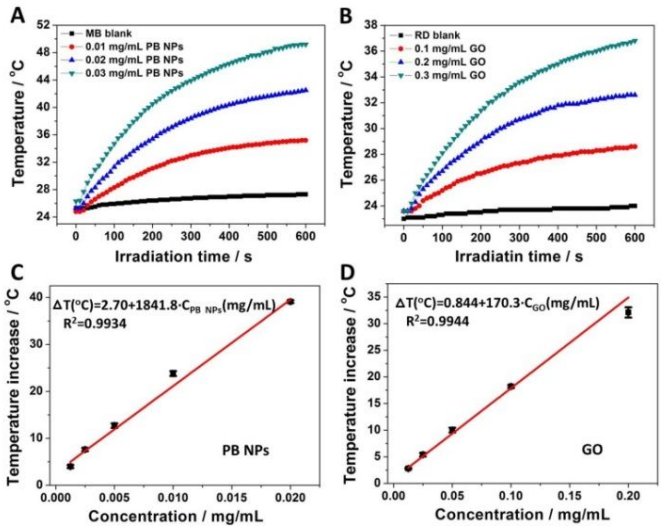

Fig. 2 Off-chip photothermal effect-induced temperature elevation of nanomaterials and dyes as a function of (A-B) irradiation time and (C-D) nanomaterial concentration. Temperature comparison among (A) different concentrations of PB NPs suspended in MB solutions (0.054 mg/mL), and (B) different concentrations of GO suspended in RD solutions during the laser irradiation process for 10 min at a power density of 3.12 W·cm^{-2}. Temperature increases (ΔT) *vs.* concentrations of (C) PB NPs suspensions and (D) GO suspensions after the laser irradiation for 1.0 min at a power density of 5.26 W·cm^{-2}. Error bars represent standard deviations (n = 4).

To investigate the relationship between the photothermal effect-induced temperature elevation and the nanomaterial concentration, the nanomaterial suspensions at different concentrations were vertically exposed to the 808 nm laser for 1.0 min. The temperature of the suspensions was immediately recorded by using a digital thermometer after the irradiation. Fig. 2C-D shows the temperature increment as a function of the nanomaterial concentration. It was found that the temperature elevation values of both PB NPs and GO suspensions were proportional to the nanomaterial concentrations in the ranges of 0.00125-0.02 mg·mL^{-1} and 0.0125-0.2 mg·mL^{-1}, respectively. It was worth noting that PB NPs exhibited a 10.8-fold higher slope than GO, further demonstrating the stronger photothermal effect of PB NPs than GO.[35]

On-chip photothermal effects of the nanomaterials

By utilizing MB and RD as the on-chip dye indicators of PB NPs and GO, respectively, the on-chip photothermal effects of the nanomaterials were investigated in a PMMA/PDMS hybrid microfluidic chip (see Chip 1 in Fig. S1). The nanomaterials were suspended in the dye solutions and then loaded in inlets of the PT-Chip, followed by sealing of the inlets with a top PDMS layer. Hence, Chip 1 preloaded with the nanomaterial-dye suspensions was assembled with only the outlets accessible to the atmosphere. To study the photothermal microfluidic pumping performance on the PT-Chip, inlets of Chip 1 were

individually exposed to the laser using blank MB and RD as the control. The photothermal pumping distance of dye indicators was quantitatively measured by using the visual on-chip ruler. As shown in Fig. 3, both PB NPs (Channel 2) and GO (Channel 4) displayed rapid and visual on-chip bar-chart pumping of the nanomaterial-dye suspensions after the laser irradiation for 50 s (see the SI for the recorded video), whereas MB (Channel 1) and RD (Channel 3) displayed no apparent bar-chart movement due to their poor photothermal effects. GO with a 10-fold higher concentration showed a 3.0-fold shorter bar-chart movement distance than PB NPs, which can be attributed to the weaker photothermal effect of GO than PB NPs, as demonstrated in Fig. 2. In contrast, PB NPs at a low concentration of 0.1 mg·mL^{-1} still resulted in a bar-chart pumping distance of 64.4 mm under the irradiation process of only 50 s, thus suggesting the robustness of the photothermal effect as the bar-chart microfluidic driving force.

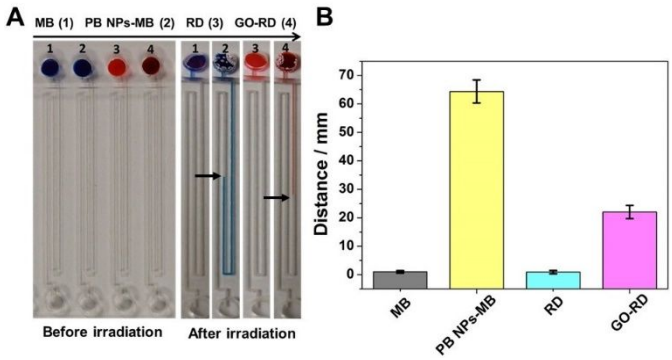

Fig. 3 On-chip photothermal microfluidic pumping performance on the PT-Chip (Chip 1). (a) Photographs of the PT-Chip loaded with blank MB, PB NPs-MB (0.1 mg·mL^{-1}), blank RD, and GO-RD (1.0 mg·mL^{-1}) suspensions before and after the laser irradiation for 50 s at a power density of 2.6 W·cm^{-2}. The black arrows indicate the endpoint of the dye bars. (b) Comparison among on-chip photothermal pumping distances after the laser irradiation. Error bars represent standard deviations (n = 4).

During the irradiation process of the nanomaterial-dye suspensions, the on-chip nanomaterial-mediated photothermal effect resulted in rapid and substantial heat production in the inlets. The subsequent heating of solutions led to the rapid accumulation of vapor pressure inside the inlets with limited volumes, thereby driving the visual bar-chart movement of the nanomaterial-dye suspensions in the channels. Therefore, a new type of bar-chart microfluidic platform, photothermal bar-chart chip (PT-Chip), was developed using the on-chip nanomaterial-mediated photothermal effect as the microfluidic driving force, as illustrated in Scheme 1A. In addition to the robustness of the photothermal microfluidic pump, another key feature of the new PT-Chip is that the on-chip photothermal pumping rate is highly tunable by remotely adjusting the parameters of the laser, whereas it is quite challenging to spatiotemporally adjust enzyme- or nanoparticle-catalyzed reactions on a chip. It was observed that the ongoing bar-chart movement can be instantly terminated upon the removal of the laser irradiation. It should be noted that the nanomaterial-mediated photothermal effect is more stable than the enzyme-catalyzed gas-production approach as the microfluidic photothermal pump, because enzymes can easily lose activity at room temperature while the photo-physical conversion efficiency is intrinsically inert to surrounding environments. Furthermore, by tuning the irradiation diameter of the laser spot and changing the layout of the chip, multiple inlets can be irradiated at one irradiation process, enabling on-demand microfluidic pumping in a multiplexed manner. These results indicated the feasibility to utilize the on-chip nanomaterial-mediated photothermal effect as a new type of robust, tunable and versatile microfluidic driving force in bar-chart chips.

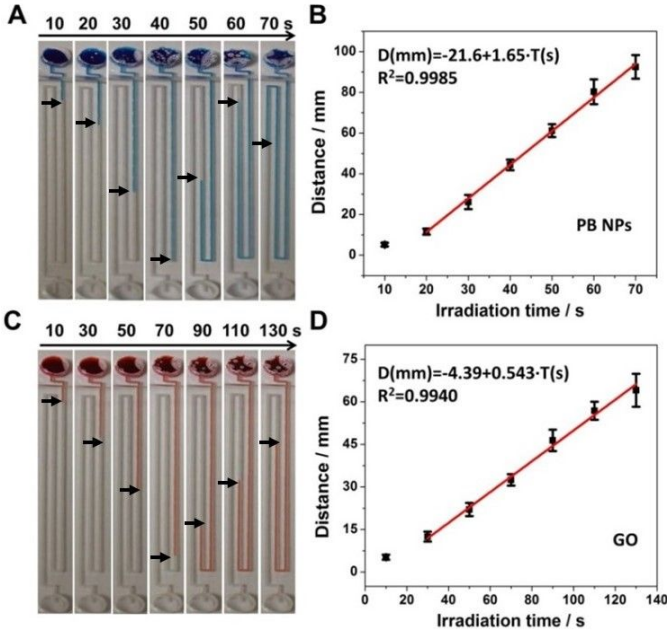

Fig. 4 Effect of laser irradiation time on photothermal microfluidic pumping performance on the PT-Chip (Chip 1). (A) Photographs of the PT-Chip loaded with PB NPs-MB suspensions (0.1 mg·mL^{-1}) after the laser irradiation for different times at 2.6 W·cm^{-2}. (B) On-chip photothermal pumping distance of the PB NPs-MB suspensions as a function of the irradiation time. (C) Photographs of the PT-Chip loaded with GO-RD suspensions (1.0 mg·mL^{-1}) after the laser irradiation for different times. (D) Photothermal pumping distance of the GO-RD suspensions as a function of the irradiation time. The black arrows indicate the endpoint of the dye bars. Error bars represent standard deviations (n = 4).

We further systematically studied other fundamental aspects of the PT-Chip. To study the influence of irradiation time on the performance of the PT-Chip, inlets of Chip 1 loaded with the same concentrations of the nanomaterial-dye suspensions were individually irradiated with the laser for different times. As shown in Fig. 4, with the increase of the irradiation time, gradually prolonged bar-chart movement distance was clearly observed in cases of both PB NPs and GO. Longer irradiation time of the nanomaterials caused the on-chip production of increasing amounts of heat, consequently leading to the progressive accumulation of increasing vapor pressure in limited volumes of the inlets. In good agreement with the result

obtained from Fig. 3, PB NPs with a 10-fold lower concentration displayed a longer bar-chart pumping distance than GO at each irradiation time. Both PB NPs and GO showed a good linear relationship between the photothermal pumping distance and the irradiation time in the ranges of 10-70 s and 10-130 s, respectively. Significantly, PB NPs exhibited a 3.0-fold higher slope than GO, implying higher photothermal microfluidic pumping efficiency of PB NPs-mediated photothermal effect than that of GO.

In addition, the effect of nanomaterial concentration on the performance of the PT-Chip was investigated, as shown in Fig. 5. Inlets preloaded with different concentrations of the nanomaterial-dye suspensions were individually irradiated for the same time. With the increase of the nanomaterial concentration, PB NPs displayed an increasingly prolonged bar-chart pumping distance that was obviously longer than GO even with 10-fold higher concentrations and longer irradiation times. Higher concentrations of the nanomaterials accordingly led to the accumulation of higher vapor pressure in the inlets as a result of the concentration-dependent photothermal effect of the nanomaterials. The bar-chart pumping distances of both PB NPs- and GO-driven PT-Chips were proportional to the concentrations of the nanomaterials in the ranges of 0.00625-0.2 mg·mL^{-1} and 0.0625-2.0 mg·mL^{-1}, respectively, which laid the basis for the quantitative application of the PT-Chips. The quantitative readout results of the microfluidic pumping performance are visually displayed as on-chip ink-bar-charts without the aid of any complex and costly analytical instruments, making it particularly advantageous for POCT.

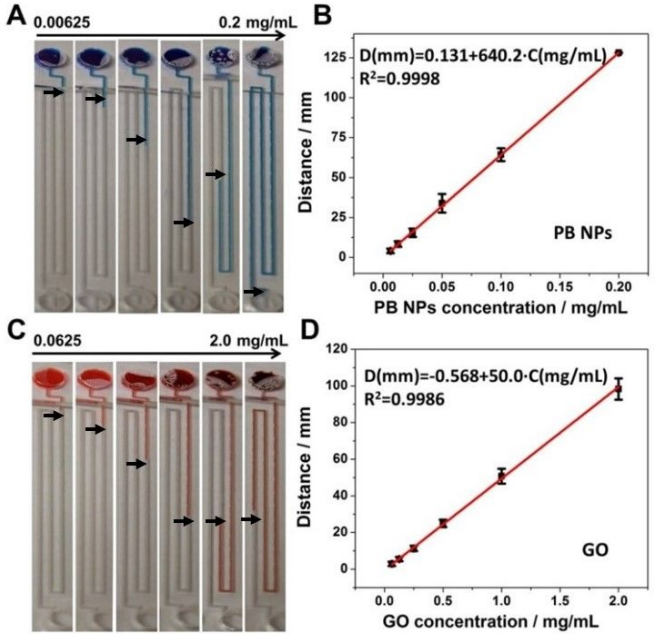

Fig. 5 Effect of nanomaterial concentration on photothermal bar-chart microfluidic pumping performance on the PT-Chip (Chip 1). (A) Photographs of the PT-Chip loaded with different concentrations of PB NPs-MB suspensions after the laser irradiation for 50 s at 2.6 W·cm^{-2}. (B) Calibration plot of bar-chart pumping distance of the PB NPs-MB suspensions *vs*. PB NPs concentration. (C) Photographs of the PT-Chip loaded with different concentrations of GO-RD suspensions after the laser irradiation for 90 s. (D) Calibration plot of bar-chart pumping distance of the GO-RD suspensions *vs*. GO concentration. The black arrows indicate the endpoint of the dye bars. Error bars represent standard deviations (n = 4).

To evaluate the reproducibility of the photothermal microfluidic pumping performance, inlets of Chip 1 preloaded with the same concentrations of the nanomaterials were individually irradiated for the same time. As shown in Fig. 6, the PT-Chips driven by both PB NPs- and GO-mediated photothermal effect displayed uniform bar-chart movement distance after the irradiation. Measurement of the bar-chart pumping distance of six parallel inlets loaded with PB NPs and GO showed low relative standard deviations (RSD) of 4.6% and 5.1%, respectively, indicating good reproducibility of the photothermal bar-chart microfluidic pumping performance on the PT-Chip.

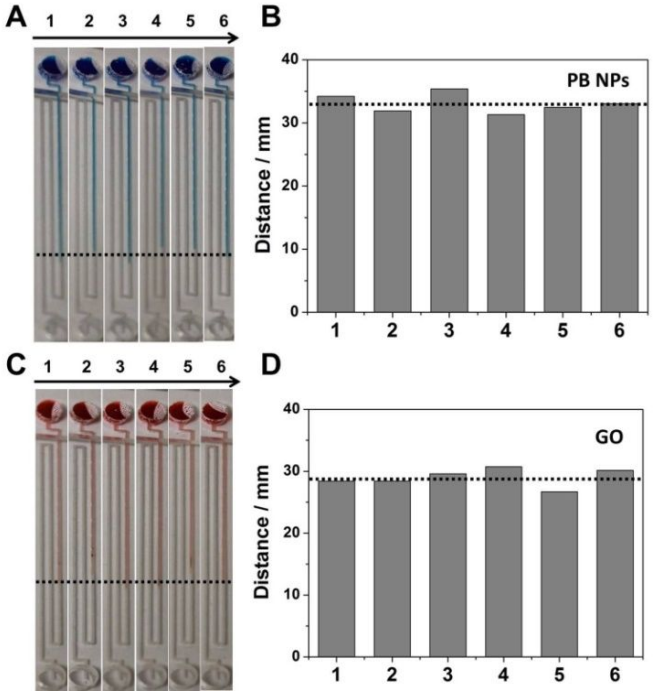

Fig. 6 Reproducibility of photothermal microfluidic pumping performance on the PT-Chip. (A) Photographs and (B) the measured bar-char pumping distance of Chip 1 loaded with the same concentration of PB NPs-MB suspensions (0.05 mg·mL^{-1}) after the laser irradiation for 50 s at 2.6 W·cm^{-2}. (C) Photographs and (D) the measured bar-chart pumping distance of Chip 1 loaded with the same concentration of GO-RD suspensions (0.5 mg·mL^{-1}) after the laser irradiation for 90 s.

Application in multiplexed on-chip transport of substances using the photothermal microfluidic pump

It has been well established that on-chip transport of fluids or substances, such as nanoparticles and chemicals, is of significant importance for various microfluidic applications.[47-49] Dye transport driven by different pumping principles is the foundation of bar-chart chips.[20] To further exemplify the application of the photothermal microfluidic pumping system, on-chip transport of substances, such as dyes and AuNPs, using

two PT-Chips (see Chip 2 and Chip 3 in Fig. S1-2) was conducted employing the photothermal microfluidic pumps.

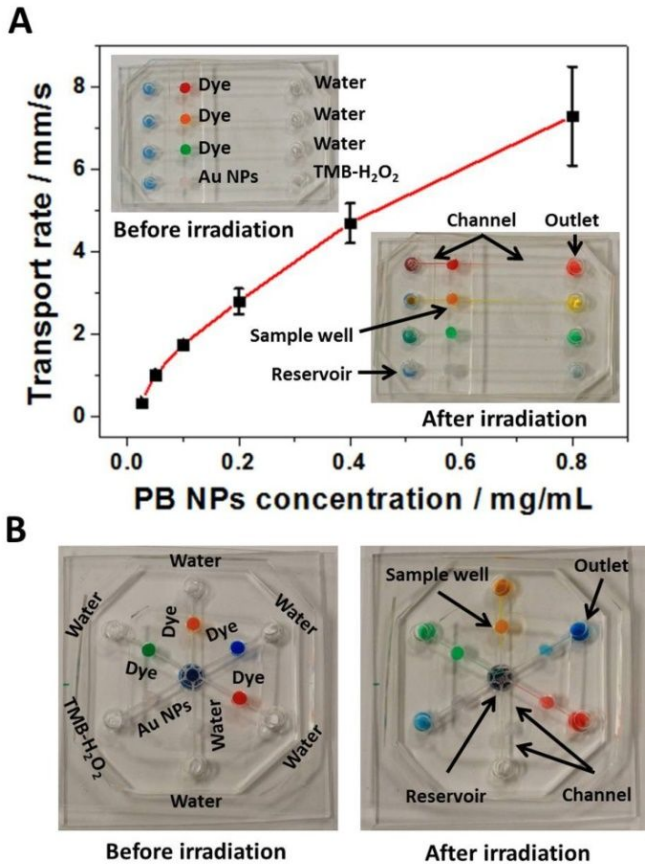

Fig. 7 Application of the photothermal microfluidic pump for on-chip transport of dyes and AuNPs. (A) On-chip transport rate as a function of PB NPs concentrations in the single-sample transport PT-Chip (Chip 2). Insets: Photographs of Chip 2 before and after the laser irradiation (2.6 $W \cdot cm^{-2}$) at a PB NPs concentration of 0.1 $mg \cdot mL^{-1}$. (B) Photographs of the multiplexed transport PT-Chip (Chip 3) before and after the laser irradiation at a PB NPs concentration of 0.4 $mg \cdot mL^{-1}$. Error bars represent standard deviations (n = 4).

On-chip single-sample transport upon one laser irradiation process was first performed using a new microfluidic PT-Chip (Chip 2) as a proof of concept. PB NPs suspensions were preloaded in reservoirs of Chip 2 and target substances were stored in middle sample wells as shown in Fig. 7A. To assess the possibility of the PT-Chip for on-chip transport of nanoparticles, the AuNPs-catalyzed TMB-H_2O_2 colorimetric reaction system was integrated on the PT-Chip. Herein, AuNPs were stored in sample wells with preloaded TMB-H_2O_2 solutions in the outlets. Owing to the AuNPs-catalyzed TMB-H_2O_2 colorimetric reaction,[50-52] the successful pumping of AuNPs to the outlets can result in visual color changes from colorless to blue. To prevent the mixing of PB NPs with target transport substances during the irradiation, PB NPs suspensions were loaded below the reservoir entrances in the third layer (i.e. the PMMA plate). Insets in Fig. 7A show the PT-Chip (Chip 2) before and after the laser irradiation of each reservoir. Upon individual irradiation of the reservoirs, dyes stored in the sample wells were pumped rapidly to the outlets through the channels, thereby displaying the corresponding color changes in the outlets. Interestingly, a clear color change from colorless to blue was also observed in the outlet loaded with TMB and H_2O_2, suggesting the successful pumping of AuNPs from the sample well to the outlet where the AuNPs-catalyzed TMB-H_2O_2 colorimetric reaction took place.[50-52] A significantly high flow rate of 1.8 $mm \cdot s^{-1}$ was achieved at a low PB NPs concentration of 0.1 $mg \cdot mL^{-1}$. It was found that the bar-chat flow rate was positively correlated with the PB NPs concentration in the range from 0.025 to 0.8 $mg \cdot mL^{-1}$. With the increase of the PB NPs concentration, increasing PB NPs-mediated photothermal effect led to the increasing vapor pressure in the reservoirs. The pressure pathway extended from the reservoir entrances to the sample wells, thus pumping target substances to move towards the outlets. These results demonstrated the successful application of the PB NPs-mediated photothermal effect as the photothermal microfluidic pump for on-chip transport of substances.

To further verify the possibility of the PT-Chip for on-chip transport of substances in a multiplexed manner, a new multiplexed PT-Chip (Chip 3) was fabricated, as shown in Fig. 7B. On this multiplexed photothermal microfluidic plumping system, one central reservoir was connected to multiple pumping pathways and samples wells through the reservoir entrance. PB NPs suspensions (80 µL, 0.4 $mg \cdot mL^{-1}$) were loaded in the central reservoir, while dyes and AuNPs (20 µL per sample well) were independently stored in six sample wells. Surprisingly, upon only one irradiation process of 2.0 min to the central reservoir, the dyes and AuNPs suspensions in all sample wells were simultaneously pumped into relevant outlets with a rapid pumping rate of 60 $\mu L \cdot min^{-1}$. Hence, the PB NPs-mediated photothermal effect achieved from only one central reservoir was sufficient to pump at least six microfluidic pathways, demonstrating great potential of the PB NPs-mediated photothermal effect for on-chip sample transport in a multiplexed manner. Similarly, as discussed in the results of Fig. 3, the on-chip transport process can be immediately terminated upon the removal of the laser irradiation. The transport rate is also highly controllable by remotely adjusting the parameters of the laser. It is cumbersome to change enzyme concentrations to control the catalytic reaction rate for gas production on a highly integrated chip. Furthermore, it is worth noting that contamination and denaturation of target samples can be effectively avoided during the on-chip transport process, since target samples are well separated from the photothermal nanomaterials in the central reservoir where only vapor pressure travels outside the reservoir through the reservoir entrance. Thus, the target samples are neither contaminated nor heated during the transport process, which is of appealing advantage for on-chip multiplexed transport of biomolecules, such as protein and DNA. In addition, both PB NPs and GO used in the PT-Chips are typical NIR laser-driven photothermal nanomaterials with simple preparation, low cost, low cytotoxicity, and synthetically modifiable photothermal properties (e.g. particle size, material shape and surface modification), making them practically adaptable for extensive

applications in the PT-Chips. Since the particle size can affect the photothermal effects, photothermal effects of different-szied nanomaterials can be further optimized to achieve desired pumping performance.

Application in visual quantitative biochemical analysis using the photothermal microfluidic bar-chart platform

To further extend the application of the photothermal bar-chart microfluidic pumping platform in visual quantitative biochemical analysis, we applied our PT-Chip for visual quantitative detection of prostate-specific antigen (PSA, a prostate cancer biomarker) based on the readout of the photothermal pump-driven movement distance of the ink bars, without using specialized instruments. As illustrated in Fig. 8A, iron oxide NPs conjugated with the detection antibody (i.e. anti-PSA antibody) were used to bridge a sandwich-type immunoassay with the photothermal sensing strategy according to our previous works.[40,41] Since the photothermal effect of captured iron oxide nanoparticles was too weak, they were converted into a strong photothermal agent, PB NPs. After the conversion, the immunosensing solutions obtained from different concentrations of the target PSA were loaded into multiple inlets of the PT-Chips, which were irradiated simultaneously by one NIR laser beam. Different amounts of PB NPs produced from the immunoassay with varying concentrations of PSA led to the on-chip generation of different amounts of heat and corresponding bar-chart pumping distances as the visual quantitative readout signals. As shown in Fig. 8B, one channel obtained from 64 ng·mL^{-1} PSA displayed a bar-chart pumping distance of 20.9 mm, while the control channel (i.e. 0 ng·mL^{-1} PSA, blank) only exhibited a negligible pumping distance. It is worthy to note that the bar-chart pumping distance was proportional to the concentration of PSA in the range from 2 ng·mL^{-1} to 64 ng·mL^{-1} upon the laser irradiation for 5 min at a power density of 2.2 W·cm^{-2}. The limit of detection (LOD) was determined to be 2.0 ng·mL^{-1} based on the signal-to-noise ratio of three, which indicated high sensitivity and capability of the PT-Chip to meet the cut-off requirement of clinical diagnostics using 4.0 ng·mL^{-1} as the threshold concentration.[34, 47] The results exemplified a new application of the nanomaterial-mediated photothermal microfluidic pumping platform, and demonstrated excellent performance of the PT-Chip for visual quantitative readout of bioassay signals, with no aid of any bulky and expensive analytical instruments (even a thermometer [40, 41]).

Herein, it should be noted that the off-chip PSA immunoassay only serves as a proof-of-concept study to prove the capability of the PT-Chip for visual quantitative readout of detection signals using the photothermal pumping principle, since the development of the photothermal bar-chart pumping platform is the major focus of the work. On the basis of the present pumping platform, we believe that various photothermal agent-involved immunoassay systems can be integrated into the PT-Chip to enable the simple on-chip visual quantitative POCT,[53] owing to the superiorities of the new microfluidic pumping platform.

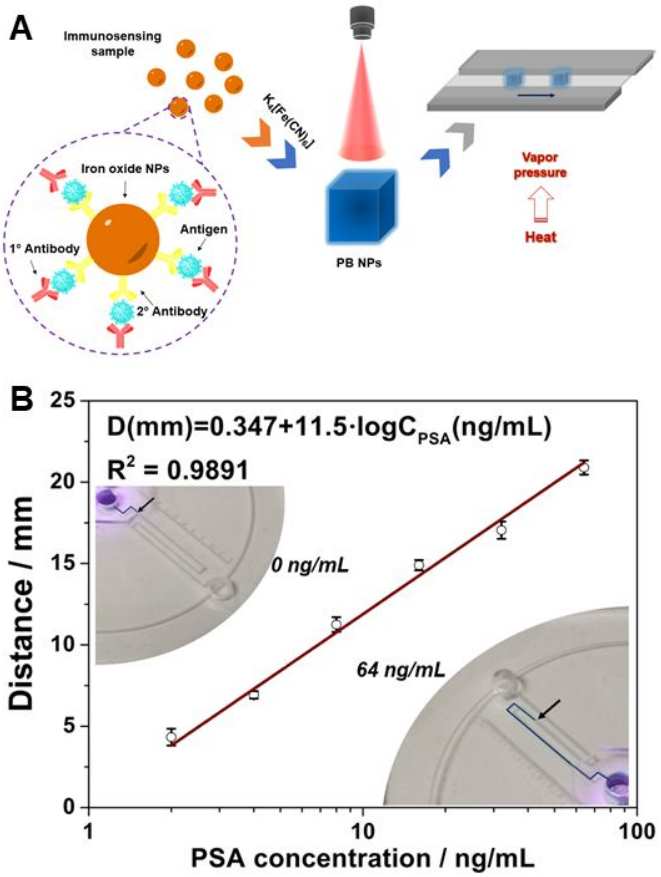

Fig. 8 Visual quantitative readout of PSA concentrations using a 4-channel PT-Chip. (A) Schematic illustration of the photothermal immunoassay including the off-chip iron oxide NPs-involved immunoassay, the conversion from iron oxide NPs to PB NPs, and the on-chip visual quantitation based on the bar-chart pumping distances. (B) The calibration curve of the on-chip detection of PSA using the measured bar-chart pumping distance with different concentrations of PSA after the laser irradiation for 5 min at 2.2 W·cm^{-2}. Inets: Photographs taken during the on-chip detection of PSA at 0 and 64 ng·mL^{-1}, respectively. Error bars represent standard deviations (n = 4).

Conclusions

We developed a new type of microfluidic pumping platform, photothermal microfluidic chip (PT-Chip), based on the integration of on-chip nanomaterial-mediated photothermal effect as the novel on-demand microfluidic driving force. We designed 3 different chips to study different fundamental aspects and demonstrated the proof of concept of the tunable PT-Chip. The remotely tunable photothermal effect of nanomaterials propelled robust on-chip bar-chart movement of dyes, enabling visual quantitative readouts and the exploration of on-chip nanomaterial-mediated photothermal effect as a new type of on-demand microfluidic pumps. We further exemplified the application of the photothermal microfluidic pump for on-chip transport of substances, such as AuNPs, by using Chip 2 and Chip 3 in a multiplexed manner. This

microfluidic photothermal pumping strategy was also applied for the visual quantitative detection of a cancer biomarker on a PT-Chip based on the visual readout of the bar-chart pumping distances, without using any specialized instruments. The LOD down to the concentration of 2.0 ng/mL PSA was achieved, meeting the sensitivity requirement in clinical diagnostics. In comparison with the traditional V-Chips using enzyme- or nanoparticle-catalyzed gas production as the driving force, the PT-Chip is particularly advantageous because of its robustness (i.e. strong and rapid photothermal conversion efficiency), remote on-demand controllability (i.e. precise controllability by remotely adjusting the laser parameters), stability (i.e. inertness of the photo-physical conversion efficiency to surrounding environments), and flexibility and versatility (i.e. applicability of a wide range of photothermal nanomaterials and small organic photothermal molecules). With the commercial availability of various affordable and powerful pen-style laser pointers, another key merit of the photothermal microfluidic pump is the portability by using a handheld laser pointer as the light source, compared with traditional pneumatic syringe pumps. Furthermore, unlike most traditional injector-based microfluidic pumping, no connecting accessories (e.g. injection syringes and tubes) are required for the PT-Chips, thus optimizing the operational space and simplicity. Our main advantages over conventional pumping lie in: 1) contact-free; 2) remotely tuneable; 3) small size; 4) less complex; 5) reagent transport in “local” regions without affecting other sections; and 6) photothermal bar-chart chip for visual quantitative biochemical analysis without using any specialized instrumentations. As far as we know, this is the first report of microfluidic pumping platform using the on-chip nanomaterial-mediated photothermal effect as the microfluidic driving force, which will have great potential for various microfluidic applications, particularly for visual quantitative POCT of various biochemicals.

Experimental section

Materials and instruments

Poly(methyl methacrylate) (PMMA, 2.0 mm in thickness) sheets were purchased from McMaster-Carr (Los Angeles, CA). Polydimethylsiloxane (PDMS, Sylgard 184) was acquired from Dow Corning (Midland, MI). Graphene oxide (GO) nanosheets were the product of Graphene Laboratories (Calverton, NY). Methylene blue (MB) and Prostate-specific antigen (PSA) were purchased from Sigma-Aldrich (St. Louis, MO). Red food dyes were obtained from Walmart (El Paso, TX). Prussian blue nanoparticles (PB NPs) were prepared according to the literature.[54, 55] All solutions and nanomaterial suspensions were prepared with ultrapure Milli-Q water (18.2 MΩ·cm) collected from a Milli-Q system (Bedford, MA). Unless otherwise stated, all other chemicals were of analytical grade and used as received. UV-Vis absorption spectroscopic characterization was carried out on a SpectraMax Multi-Mode Microplate Reader (Molecular Devices, LLC, Sunnyvale, CA) utilizing a 96-well microplate. The temperature of the suspensions was measured by using a digital thermometer (KT-300 LCD) with a detection range of -50 to +300 °C. The 808 nm diode laser (MDL-III-808) with an output power (PSU-III-LED) adjustable from 0 W to 2.5 W was obtained from Opto Engine LLC (Midvale, UT).

Design and fabrication of the PMMA/PDMS hybrid photothermal microfluidic chips

We designed three chips (see Fig. S1) to demonstrate the versatile applications of the PT-Chips. Patterns of these chips were designed with the Adobe Illustrator CS5 software, followed by laser ablation of the PMMA/PDMS sheets by employing a laser cutter (Epilog Zing 16, Golden, CO). As shown in Fig. S1, the PT-Chip (**Chip 1)** was composed of three layers including a bottom PMMA plate (2.0 mm in thickness), a middle PDMS slice (4.0 mm in thickness), and a top PDMS sealing slice (2.0 mm in thickness). Channels with a width of 0.25 mm and inlets with a diameter of 3.0 mm were created on the bottom PMMA plate by employing the laser cutter. The fabrication parameters (*e.g.*, speed: power intensity) for channels and inlets were 40: 40% and 25: 50%, respectively. An on-chip ruler for measurement of the bar-chart pumping distance was carved on the bottom PMMA plate. Inlets and outlets with a diameter of 3.0 mm were thoroughly punched in the middle PDMS slice by using a puncher (Harris, USA). Both PMMA plates and PDMS slices were thoroughly washed before the chip assembly, followed by the treatment with a plasma cleaner (PDC-32 G) for 30 seconds. To fabricate the PMMA/PDMS hybrid microfluidic chips, the bottom PMMA plate with patterns facing up was coated by the middle PDMS slice. The two layers were aligned to overlap corresponding wells. The nanomaterials (PB NPs and GO) were first suspended in aqueous solutions of the dyes (i.e. MB and RD) and then preloaded in inlets (20 μL) of the chips. The inlets were ultimately sealed with the top PDMS slice.

Design and fabrication of the photothermal microfluidic transport chip

The single-sample transport chip (**Chip 2**) was fabricated with five layers: 1) a bottom PMMA plate (2.0 mm in thickness) with superficially carved reservoirs and outlets facing up; 2) a PDMS slice (4.0 mm in thickness) as the second layer with thoroughly punched reservoirs and outlets; 3) another PMMA plate as the third layer with thoroughly carved outlets and reservoir entrances (3.0 mm in diameter), and superficially carved patterns with channels and sample wells facing up; 4) a PDMS slice (4.0 mm in thickness) with thoroughly punched sample wells and outlets as the fourth layer; 5) another PDMS slice (2.0 mm in thickness) as the top sealing layer of the sample wells. All reservoirs and outlets were in the same diameter of 6.0 mm. The diameter of all sample wells was 4.0 mm. The width of channels on the PMMA plate (i.e. the third layer) was 0.25 mm. All layers were sequentially assembled together from bottom to top by aligning corresponding wells. PB NPs suspensions (40 μL per well) were injected into reservoirs through the reservoir entrances after assembling the third layer. Target samples (20 μL), such as dyes and AuNPs, were preloaded in the sample wells after assembling the fourth layer. The multiplexed transport chip (**Chip 3**) was fabricated according to the same

protocol as mentioned above except the major difference in one central reservoir shared with six channels in this chip. Six sample wells were connected to one central reservoir entrance.

Off-chip and on-chip investigation of photothermal effects of nanomaterials

To investigate the off-chip photothermal effect of PB NPs and GO, the temperature changes of both suspensions were monitored during the laser irradiation process. Different concentrations of the nanomaterial suspensions (1.0 mL) in disposable UV cuvettes were horizontally exposed to the laser at a power density of 3.12 $W \cdot cm^{-2}$ for 10 min. A digital thermometer was inserted into the suspensions to monitor the temperature change. For the further quantitative off-chip photothermal investigation, PCR tubes with different concentrations of the nanomaterial suspensions (0.1 mL) were vertically irradiated by the laser at a power density of 5.26 $W \cdot cm^{-2}$ for 1.0 min. The temperature of the suspensions was measured by using the digital thermometer immediately after the irradiation. It should be noted that the laser irradiation intensity changed (3.12 or 5.26 $W \cdot cm^{-2}$) due to different laser irradiation directions and varying surface areas in different measurement situations. To study the on-chip photothermal effect of the nanomaterials, inlets preloaded with different concentrations of the nanomaterial-dyes suspensions (20 µL per well) were individually irradiated by the laser at a power density of 2.6 $W \cdot cm^{-2}$ for different times. To record the on-chip bar-chart pumping distance, pictures of the chips were immediately taken upon the termination of the laser irradiation by using a camera (Canon EOS 600D) or a smartphone camera. The bar-chart pumping distance of the dyes was quantitatively measured by using the on-chip ruler.

On-chip transport of substances using the photothermal microfluidic pump

For on-chip (Chip 2) single-sample transport, reservoirs preloaded with different concentrations of PB NPs suspensions (40 µL per well) were individually irradiated by the laser at a power density of 2.6 $W \cdot cm^{-2}$ for different times. Pictures of the chips were immediately taken after the irradiation. The pumping time and pumping distance of target samples from sample wells to outlets were accurately recorded to calculate the transport rate. For the multiplexed transport chip (**Chip 3**), central reservoirs preloaded with PB NPs suspensions (80 µL, 0.4 $mg \cdot mL^{-1}$) were irradiated for 2.0 minutes at a power density of 2.6 $W \cdot cm^{-2}$. The platform setup is shown in Fig. S3 including the laser and a PT-Chip.

Visual quantitative detection of PSA on the PT-Chip based on bar-chart movement distance

The procedures (see details in ESI) for a sandwich-type immunoassay for PSA detection and the material conversion of iron oxide NPs to PB NPs were performed according to our previously published paper.[40] Each reservoir on the PT-Chip was loaded with 30 µL of immunosensing solutions, and four reservoirs were then irradiated simultaneously under an 808 nm NIR diode laser for 5 min at a power density of 2.2 $W \cdot cm^{-2}$. The visual quantitative detection of PSA on the PT-Chip was achieved by simply recording the bar-chart pumping distances of the immunosensing solutions (see details in ESI).

Conflicts of interest

The authors declare no conflict of interest.

Acknowledgements

We would like to acknowledge the financial support from the National Institute of Allergy and Infectious Disease of the NIH (R21AI107415), the U.S. NSF (IIP 1953841 and DMR 1827745), the Philadelphia Foundation, and the Medical Center of the Americas Foundation. Financial support to our research from the National Institute of General Medical Sciences of the NIH (SC2GM105584), the NIH RCMI Pilot grant, University of Texas (UT) System for the STARS award, and the University of Texas at El Paso (UTEP) for the IDR Program, Multidisciplinary Research Award Program (MRAP) and URI Program is also greatly acknowledged.

References

1. M. Dou, S. T. Sanjay, D. C. Dominguez, S. Zhan and X. Li, *Chem. Comm.*, 2017, **53**, 10886-10889.
2. M. Dou, J. M. Garcia, S. Zhan and X. Li, *Chem. Comm.*, 2016, **52**, 3470-3473.
3. M. Dou, D. C. Dominguez, X. Li, J. Sanchez and G. Scott, *Anal. Chem.*, 2014, **86**, 7978-7986.
4. P. Zuo, X. Li, D. C. Dominguez and B.-C. Ye, *Lab Chip*, 2013, **13**, 3921-3928.
5. J. Zhang, X. Wei, R. Zeng, F. Xu and X. Li, *Future Sci. OA*, 2017, **3**, FSO187.
6. S. T. Sanjay, M. Dou, G. Fu, F. Xu and X. Li, *Curr. Pharm. Biotechnol.*, 2016, **17**, 772-787.
7. Y. Ma, Y. Mao, D. Huang, Z. He, J. Yan, T. Tian, Y. Shi, Y. Song, X. Li, Z. Zhu, L. Zhou and C. J. Yang, *Lab Chip*, 2016, **16**, 3097-3104.
8. M. Dou, S. T. Sanjay, M. Benhabib, F. Xu and X. Li, *Talanta*, 2015, **145**, 43-54.
9. S. T. Sanjay, G. Fu, M. Dou, F. Xu, R. Liu, H. Qi and X. Li, *Analyst*, 2015, **140**, 7062-7081.
10. M. Dou, S. T. Sanjay, D. C. Dominguez, P. Liu, F. Xu and X. Li, *Biosens. Bioelectron.*, 2017, **87**, 865-873.
11. S. T. Sanjay, M. Dou, J. Sun and X. Li, *Sci. Rep.*, 2016, **6**, 30474.
12. M. Dou, J. Sanchez, H. Tavakoli, J. E. Gonzalez, J. Sun, J. Dien Bard and X. Li, *Anal. Chim. Acta*, 2019, **1065**, 71-78.
13. M. Dou, N. Macias, F. Shen, J. D. Bard, D. C. Dominguez and X. Li, *EClinicalMedicine*, 2019, **8**, 72-77.
14. X. J. Li and Y. Zhou, *Microfluidic Devices for Biomedical Applications*, Woodhead Publishing, 2013.
15. H. Tavakoli, W. Zhou, L. Ma, S. Perez, A. Ibarra, F. Xu, S. H. Zhan and X. J. Li, *Trac-Trend. Anal. Chem.*, 2019, **117**, 13-26.
16. S. T. Sanjay, W. Zhou, M. Dou, H. Tavakoli, L. Ma, F. Xu and X. Li, *Adv. Drug Deliver. Rev.*, 2018, **128**, 3-28.
17. Y. Song, Y. Zhang, P. E. Bernard, J. M. Reuben, N. T. Ueno,

R. B. Arlinghaus, Y. Zu and L. Qin, *Nat. Commun.*, 2012, **3**, 1283.
18. Y. Li, J. Xuan, Y. Song, P. Wang and L. Qin, *Lab Chip*, 2015, **15**, 3300-3306.
19. X. Wei, T. Tian, S. Jia, Z. Zhu, Y. Ma, J. Sun, Z. Lin and C. J. Yang, *Anal. Chem.*, 2016, **88**, 2345-2352.
20. X. Wei, W. Zhou, S. T. Sanjay, J. Zhang, Q. Jin, F. Xu, D. C. Dominguez and X. Li, *Anal. Chem.*, 2018, **90**, 9888-9896.
21. Y. Li, J. Xuan, T. Xia, X. Han, Y. Song, Z. Cao, X. Jiang, Y. Guo, P. Wang and L. Qin, *Anal. Chem.*, 2015, **87**, 3771-3777.
22. Z. Zhu, Z. Guan, S. Jia, Z. Lei, S. Lin, H. Zhang, Y. Ma, Z. Q. Tian and C. J. Yang, *Angew. Chem. Int. Ed. Engl.*, 2014, **53**, 12503-12507.
23. Y. Song, X. Xia, X. Wu, P. Wang and L. Qin, *Angew. Chem. Int. Ed. Engl.*, 2014, **53**, 12451-12455.
24. Y. Song, Y. Wang, W. Qi, Y. Li, J. Xuan, P. Wang and L. Qin, *Lab Chip*, 2016, **16**, 2955-2962.
25. Y. Song, Y. Wang and L. Qin, *J. Am. Chem. Soc.*, 2013, **135**, 16785-16788.
26. Y. Wang, G. Zhu, W. Qi, Y. Li and Y. Song, *Biosens. Bioelectron.*, 2016, **85**, 777-784.
27. S. K. Katla, J. Zhang, E. Castro, R. A. Bernal and X. Li, *ACS Appl. Mater. Interfaces*, 2018, **10**, 75-82.
28. X. Chen, Y. Chen, M. Yan and M. Qiu, *ACS Nano*, 2012, **6**, 2550-2557.
29. J. P. Yang, D. K. Shen, L. Zhou, W. Li, X. M. Li, C. Yao, R. Wang, A. M. El-Toni, F. Zhang and D. Y. Zhao, *Chem. Mater.*, 2013, **25**, 3030-3037.
30. P. Huang, J. Lin, W. Li, P. Rong, Z. Wang, S. Wang, X. Wang, X. Sun, M. Aronova, G. Niu, R. D. Leapman, Z. Nie and X. Chen, *Angew. Chem. Int. Ed. Engl.*, 2013, **52**, 13958-13964.
31. K. Yang, H. Xu, L. Cheng, C. Y. Sun, J. Wang and Z. Liu, *Adv. Mater.*, 2012, **24**, 5586-5592.
32. S. Fazal, A. Jayasree, S. Sasidharan, M. Koyakutty, S. V. Nair and D. Menon, *ACS Appl. Mater. Interfaces*, 2014, **6**, 8080-8089.
33. R. C. Lv, P. P. Yang, F. He, S. L. Gai, G. X. Yang and J. Lin, *Chem. Mater.*, 2015, **27**, 483-496.
34. M. Lin, D. D. Wang, S. W. Liu, T. T. Huang, B. Sun, Y. Cui, D. Q. Zhang, H. C. Sun, H. Zhang, H. Sun and B. Yang, *ACS Appl. Mater. Interfaces*, 2015, **7**, 20801-20812.
35. G. Fu, W. Liu, S. Feng and X. Yue, *Chem. Commun.*, 2012, **48**, 11567-11569.
36. G. Fu, W. Liu, Y. Li, Y. Jin, L. Jiang, X. Liang, S. Feng and Z. Dai, *Bioconjug. Chem.*, 2014, **25**, 1655-1663.
37. H. K. Moon, S. H. Lee and H. C. Choi, *ACS Nano*, 2009, **3**, 3707-3713.
38. H. T. Ke, J. R. Wang, Z. F. Dai, Y. S. Jin, E. Z. Qu, Z. W. Xing, C. X. Guo, X. L. Yue and J. B. Liu, *Angew. Chem. Int. Ed.*, 2011, **50**, 3017-3021.
39. X. D. Li, X. L. Liang, F. Ma, L. J. Jing, L. Lin, Y. B. Yang, S. S. Feng, G. L. Fu, X. L. Yue and Z. F. Dai, *Colloid. Surface. B,* 2014, **123**, 629-638.
40. G. Fu, S. T. Sanjay, M. Dou and X. Li, *Nanoscale*, 2016, **8**, 5422-5427.
41. G. Fu, S. T. Sanjay, W. Zhou, R. A. Brekken, R. A. Kirken and X. Li, *Anal. Chem.*, 2018, **90**, 5930-5937.
42. J. Zhang, H. Xing and Y. Lu, *Chem. Sci.*, 2018, **9**, 3906-3910.
43. W. Zhou, K. Hu, S. Kwee, L. Tang, Z. Wang, J. Xia and X. Li, *Anal. Chem.*, 2020, **92**, 2739-2747.
44. M. C. Wu, A. R. Deokar, J. H. Liao, P. Y. Shih and Y. C. Ling, *ACS Nano*, 2013, **7**, 1281-1290.
45. J. T. Robinson, S. M. Tabakman, Y. Liang, H. Wang, H. S. Casalongue, D. Vinh and H. Dai, *J. Am. Chem. Soc.*, 2011, **133**, 6825-6831.
46. G. Fu, S. T. Sanjay and X. Li, *Analyst*, 2016, **141**, 3883-3889.
47. P. Marmottant and S. Hilgenfeldt, *Proc. Natl. Acad. Sci. U. S. A.*, 2004, **101**, 9523-9527.
48. H. Obata, T. Kuji, K. Kojima, F. Sassa, M. Yokokawa, K. Takekosh and H. Suzuki, *Acs Sens.*, 2016, **1**, 190-196.
49. R. H. Lahr, G. C. Wallace and P. J. Vikesland, *ACS Appl. Mater. Interfaces*, 2015, **7**, 9139-9146.
50. X. Jiang, C. Sun, Y. Guo, G. Nie and L. Xu, *Biosens. Bioelectron.*, 2015, **64**, 165-170.
51. Y. J. Long, Y. F. Li, Y. Liu, J. J. Zheng, J. Tang and C. Z. Huang, *Chem. Commun.*, 2011, **47**, 11939-11941.
52. X. X. Wang, Q. Wu, Z. Shan and Q. M. Huang, *Biosens. Bioelectron.*, 2011, **26**, 3614-3619.
53. Z. Li, H. Chen and P. Wang, *Analyst*, 2019, **144**, 3314-3322.
54. M. Shokouhimehr, E. S. Soehnlen, J. H. Hao, M. Griswold, C. Flask, X. D. Fan, J. P. Basilion, S. Basu and S. P. D. Huang, *J. Mater. Chem.*, 2010, **20**, 5251-5259.
55. M. Shokouhimehr, E. S. Soehnlen, A. Khitrin, S. Basu and S. P. D. Huang, *Inorg. Chem. Commun.*, 2010, **13**, 58-61.

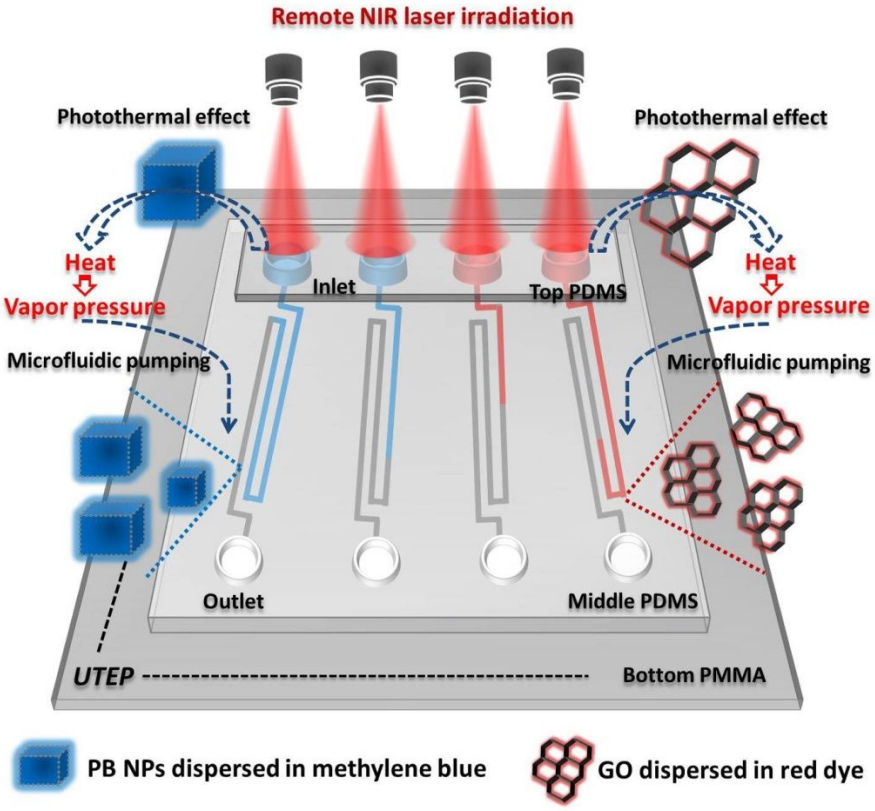

A novel on-demand photothermal microfluidic pumping platform is developed using the nanomaterial-mediated photothermal effect as the tunable microfluidic driving force.